Open Access Full Text Article

ORIGINAL RESEARCH

Nanodrugs Reprogram Cancer-Associated Fibroblasts and Normalize Tumor Vasculatures for Sequentially Enhancing Photodynamic Therapy of Hepatocellular Carcinoma

Bingyuan Fei[1,*], Zhanhao Mo[2,*], Jinghui Yang[3], Zheng Wang[4], Shuo Li[3]

[1]Department of Gastrointestinal Colorectal Surgery, China-Japan Union Hospital of Jilin University, Changchun, Jilin, People's Republic of China; [2]Department of Radiology, China-Japan Union Hospital of Jilin University, Changchun, Jilin, People's Republic of China; [3]Department of Hepatobiliary and Pancreatic Surgery, China-Japan Union Hospital of Jilin University, Changchun, Jilin, People's Republic of China; [4]CAS Key Laboratory of Nano-Bio Interface Suzhou Institute of Nano-Tech and Nano-Bionics, Chinese Academy of Sciences, Suzhou, Jiangsu, People's Republic of China

*These authors contributed equally to this work

Correspondence: Shuo Li, Department of Hepatobiliary and Pancreatic Surgery, China-Japan Union Hospital of Jilin University, Changchun, 130033, People's Republic of China, Email lishuo0609@jlu.edu.cn; Zheng Wang, CAS Key Laboratory of Nano-Bio Interface Suzhou Institute of Nano-Tech and Nano-Bionics, Chinese Academy of Sciences, Suzhou, Jiangsu, 215123, People's Republic of China, Email zwang2021@sinano.ac.cn

Background: The failure of cancer photodynamic therapy (PDT) is largely ascribed to excessive stroma and defective vasculatures that restrain the photosensitizer permeation and the oxygen perfusion in tumors.

Method and Results: In this study, a nanodrug that integrated the cancer-associated fibroblast (CAF) regulation with tumor vessel normalization was tailored to sequentially sensitize PDT. The nanodrug exhibited high targeting towards CAFs and efficiently reversed the activated CAFs into quiescence, thus decreasing collagen deposition in the tumor microenvironment (TME), which overcame the protective physical barrier. Furthermore, the nanodrug regulated vascular endothelial cells and restored the tumor vasculatures, thereby improving vascular permeability. Based on the combined effects of reprogramming the TME, the nanodrug improved tumor accumulation of photosensitizers and alleviated hypoxia in the TME, which facilitated the subsequent PDT. Importantly, the nanodrug regulated the immunosuppressive TME by favoring the infiltration of immunostimulatory cells over immunosuppressive cells, which potentiated the PDT-induced immune response.

Conclusion: Our work demonstrates a sequential treatment strategy in which the combination of the CAF regulation and tumor vasculature normalization, followed by PDT, could be a promising modality for sensitizing tumor to PDT.

Keywords: tumor microenvironment, cancer-associated fibroblast, tumor vessel, photodynamic therapy, sequential treatments

Introduction

Hepatocellular carcinoma (HCC) has become one of the most frequent primary liver malignancies and is a leading cause of cancer-related mortality worldwide.[1–3] Conventional therapies, such as hepatic resection, radiotherapy and chemotherapy remain unsatisfactory.[4,5] As an alternative, photodynamic therapy (PDT), which depends on the reaction of light-excited photosensitizers with oxygen to generate cytotoxic reactive oxygen species (ROS) to destroy tumor cells, has attracted significant attention because of the controllable, facile and noninvasive characteristics.[6,7] Moreover, PDT has been proven effective in improving tumoral immunogenicity by inducing immunogenic cell death (ICD) to recruit and alert immune cells to combat cancer metastasis.[8,9] Although promising, the efficacy of PDT is greatly restricted by the low availability of oxygen, and the limited penetration of photosensitizers and lymphocytes inside tumors due to aberrant tumor physiological and mechanical microenvironments.[10–12] These obstacles have encouraged us to develop sophisticated strategies to regulate the tumor microenvironment (TME) to achieve breakthroughs in cancer PDT.

Unlike normal vessels, tumor blood vessels are structurally and functionally abnormal, including heterogeneous tortuosity, dilation and distribution, and insufficient blood flow; this leads to a malignant TME of hypoxia, acidity and high interstitial pressure for tumor progression.[13–15] Vascular normalization therapy by targeting VEGF/VEGFR2 pathway can reverse the abnormalities in tumor vessels to promote drug delivery, immune cell infiltration and oxygen perfusion, thus having excellent potential in sensitizing PDT.[16–18] Nevertheless, single vascular normalization therapy is incomplete and has a short-lived normalization window, which causes the tumor blood vessels to quickly return to their original state.[19] The main reason for this might be the lack of TME regulation to inhibit the interaction between tumor blood vessels and the TME. Cancer-associated fibroblasts (CAFs) are among the most critical TME cells that cannot only crosstalk with cancer cells by secreting various cytokines to exert a critical tumor-promoting effect but also act as extracellular matrix (ECM) producers to generate a guarding barrier to prevent the transport of drugs and immune cells into tumors through surrounding cancer cells and secreting ECM.[20,21] Furthermore, CAFs can also deteriorate the aberrant tumor mechanical microenvironment, including increasing the solid stress and mechanical forces, to compress blood vessels, which aggravates hypoxia and distortion of blood vessels inside tumors.[22,23] Therefore, the combination of vascular normalization therapy and CAF regulation promises a synergistic effect in alleviating hypoxia and improving the permeation of drugs and lymphocytes in tumors. However, the utility of this combination strategy for PDT sensitization has not yet been explored.

Here, we propose a sequential treatment regimen that remodels the TME followed by PDT for HCC therapy (Scheme 1). The strategy of TME regulation involves retinoic acid (RA), a small molecule derived from vitamin A that reverses the activated CAFs, and gambogic acid (GA) as VEGF/VEGFR2 inhibitors that normalizes tumor blood vessels. CAF-targeted mesoporous silica nanocarriers (MSNs) were tailored to co-load RA and GA to facilitate
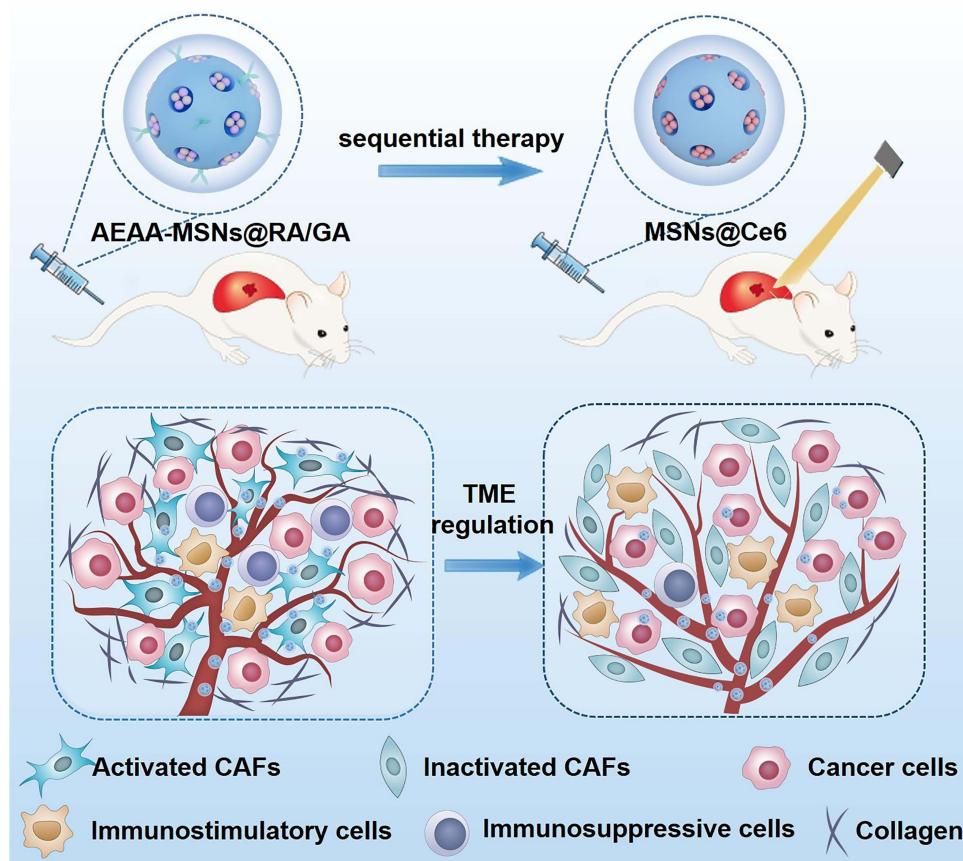
Scheme I Nanodrugs relieve tumor hypoxia, improve tumor permeation of photosensitizers and alleviate immunosuppressive TME through reversing activated CAFs and normalizing tumor vasculatures, which enhances PDT of hepatocellular carcinoma in a sequential manner.

their delivery and improve their bioavailability. Owing to the combined effects of reprogramming the TME, the nanodrugs effectively overcame the physical barrier formed by the deposited collagen and abnormal vessels, thus alleviating the hypoxic TME and improving tumor permeability. More importantly, nanodrugs improved the PDT-induced immune response by improving the infiltration of immunostimulatory cells while decreasing the number of immunosuppressive cells. Based on these multiple efficacies, the nanodrugs showed a high effect in sensitizing the PDT along with the low systemic toxicity. Our work also found that sequential treatment with TME regulation followed by PDT had a better therapeutic effect than synchronous treatments, providing a promising strategy for HCC treatments.

Materials and Methods

Synthesis of MSNs

MSNs were prepared by using a modified sol–gel approach. Briefly, we successively added 0.15 g triethanolamine (TEAH$_3$), 0.5 g cetyltrimethyl ammonium bromide (CTAB) and 50 mL deionized water into a round-bottom flask, and the mixture was stirred in the round-bottom flask at 80 °C for 30 min. Then, 5.0 g tetraethyl orthosilicate (TEOS) were slowly added into the solution and reacted at 80 °C for another 6 h. Then, the resulting products were obtained by centrifugation at 8000 r/min for 10 min and repeatedly washed with ethanol. To extract the CTAB to form mesopores, the products were refluxed at 105 °C in 1% w/v ethanol solution of NH$_4$NO$_3$ for 6 h. Then, the prepared MSNs were collected and dried for further use.

Modification of AEAA

For the amino group modification, 100 mg MSNs were dispersed in the 100 mL ethanol. The solution was heated to 80 °C and stirred for 2 h. Then, the solution was cooled to room temperature. Next, 100 μL 3-aminopropyltriethoxysilane (APTES) was added dropwise into the above solution. The mixture was refluxed at 105 °C for 6 h. Then, the amino-modified MSN (MSNs-NH$_2$) were obtained after centrifugation and washed with ethanol. To modify the AEAA on the surface of MSNs, an EDC/NHS aqueous solution was mixed with the 10 mg MSNs-NH$_2$ suspension with stirring for 30 min. Then, 5 mg COOH-PEG-AEAA was added into the mixture and reacted for another 24 h. Then, AEAA-MSNs were collected by centrifugation at 8000 rpm, washed with ethyl alcohol and deionized water three times and stored at 4 °C for further application.

Loading and Release of RA and GA

To preload RA and GA, 10 mg RA and 10 mg GA were dissolved in the 10 mL dimethyl sulfoxide (DMSO). Then, 10 mg MSNs were dispersed in the 10 mL of DMSO solution of RA and GA. After stirring at room temperature overnight, the supernatant was collected. The amounts of RA and GA in the supernatant were measured by using high-performance liquid chromatography (HPLC). The drug loading content was determined using the equation: Drug loading content (%) = Mass of drug in NPs/Mass of drug loaded NPs. To explore the drug release properties, AEAA-MSNs@RA/GA was transferred into a dialysis bag and placed in PBS solution (pH 5.5 and Ph 7.4) with stirring. Then, RA and GA in the supernatant were collected at the predetermined time points, and the amounts of RA and GA in the supernatant were measured by HPLC.

Preparation of MSNs@Ce6

Ten-milligram MSNs-NH$_2$ was dissolved in the 10 mL deionized water. Then, 5 mg chlorine e6 (Ce6) was added into the MSN-NH$_2$ solution and stirred at room temperature for 24 h. The products were collected by centrifugation at 8000 rpm/min and washed with deionized water for further use. For PEGylation, the resulting products were added with an EDC/NHS aqueous solution and subsequently added with 5 mg COOH-PEG. After reaction at room temperature for another 24 h, Ce6-loaded PEGylated MSNs (MSNs@Ce6) were collected by centrifugation.

Cell Culture

H22 hepatocellular carcinoma cell lines were cultured in RPMI 1640 supplemented with 10% fetal calf serum (FCS). Mouse NIH/3T3 fibroblast cell lines were cultured in a 1:1 mixture of Dulbecco's modified Eagle's medium with Ham's nutrient mixture F-12 containing 2 mM glutamine. Human umbilical vein endothelial cell lines (HUVECs) were maintained in Iscove's Modified Dulbecco medium (IMDM) supplemented with 20% (v/v) FBS. No ethics committee

permission was needed for the use of these cells because these cells were certified by the ATCC. To generate CAFs, NIH/3T3 cells were cultured in a 10-cm plate at a density of 1×10^6 cells/well overnight. Then, these NIH/3T3 cells were incubated with 10 ng/mL TGF-β1 for another 72 h to induce the CAF differentiation. The specific mRNA of CAFs including α-SMA and FAP-α was detected by qPCR.

CAF-Targeting Evaluation

To investigate the cellular uptake behavior, Cy 5.5-labeled MSNs or AEAA-MSNs (12.5 μg/mL) were incubated with CAFs or H22 cells for 6 h. Then, these cells were stained with DAPI for 15 min and detected by using the confocal laser scanning microscopy (CLSM; Olympus FV1000; Olympus, Tokyo, Japan). To quantify the cellular internalization, these cells were resuspended for fluorescence-activated cell sorting (FACS), and the fluorescent signals were detected using flow cytometry (BD Biosciences, Franklin Lakes, NJ, USA).

Cytotoxicity Assessment

H22 cells, CAFs and HUVECs were seeded into 96 well plates overnight (5×10^3 cells/well). Then, various concentrations of AEAA-MSNs or AEAA-MSNs@RA/GA were added into these cells and co-incubated for 24 h. Then, the cell viability was measured using a sulforhodamine B (SRB) assay. To explore the PDT effect of MSNs@Ce6, H22 cells were incubated with various concentration of MSNs@Ce6 for 24 h and exposed with the laser (660 nm, 0.1 W/cm^2) for 5 min. Then, the cell viability was measured by using SRB assay.

CAF Reprogramming

CAF cells were cultured into 6-well plate overnight (5×10^5 cells/well). Subsequently, these cells were treated with free RA, free GA, AEAA-MSNs, AEAA-MSNs@RA, AEAA-MSNs@GA or AEAA-MSNs@RA/GA (12.5 μg/mL) for 24 h. Then, the specific mRNA of CAFs including α-SMA and FAP-α was detected by qPCR.

Animal Models

Twenty-gram male ICR mice were obtained from the Jilin University Animal Experimental Center and raised in a traditional animal housing facility. The animal experimental protocols were permitted by the Ethics Committee of Jilin University Animal Experimental Center. All the animal operation accord with the National Institute of Health Guide for the Care and Use of Laboratory Animals. To establish CAFs-rich H22 tumor models, 4×10^6 H22 cells, and 1×10^6 cell were mixed and injected into the right shoulder of mice until the tumor volume reached approximately 80 mm^3.

TME Reprogramming

The CAFs-rich H22 tumor-bearing mice was intravenously injected with saline, AEAA-MSNs, AEAA-MSNs@RA, AEAA-MSNs@GA or AEAA-MSNs@RA/GA (5 mg/kg) every 3 days for total four administrations, respectively. During the next 11 days, all the mice were sacrificed, and the tumors were harvested to prepare sections. Rabbit anti-α-SMA (1:100 dilution, Abcam) and rabbit anti-FAP-α antibody (1:100 dilution; Abcam) were used for immunohistochemistry (IHC) analysis. The Masson's trichrome assay was carried out to measure the collagen existing in the TME. The tumor slices were stained with a Masson's trichrome kit and imaged by an Eclipse Ti-U inverted microscope (Nikon Corp, Japan). To detect the hypoxia, the tumors were sliced, stained with anti-pimonidazole antibodies (mouse FITC-MAb 1:50, Hypoxyprobe, Inc.) and observed with a fluorescence microscope.

Tumor Accumulation of Nanophotosensitizers

CAF-rich H22 tumor-bearing mice were intravenously injected with saline, AEAA-MSNs, AEAA-MSNs@RA, AEAA-MSNs@GA, or AEAA-MSNs@RA/GA (5 mg/kg) on days 0, 3, 6, and 9, and then intravenously injected with Cy 5.5 - labeled MSNs@Ce6 on day 11. The tumors were harvested 2, 6, 12, 24, and 48 h after MSNs@Ce6 administration and homogenized to detect fluorescence signals from MSNs@Ce6 in the tumors.

## Antitumor Effect and Biosafety in vivo

The CAF-rich H22 tumor models were randomized into the five groups and then administrated with saline, MSNs@Ce6 (10 mg/kg) +Laser, AEAA-MSNs@RA/GA (10 mg/kg), AEAA-MSNs@RA/GA (10 mg/kg) simultaneously combined with MSNs@Ce6 (10 mg/kg) +Laser, and AEAA-MSNs@RA/GA (10 mg/kg) sequentially combined with MSNs@Ce6 (10 mg/kg) +Laser. In the laser irradiation group, the tumor was irradiated by the laser (660 nm, 0.1 W/cm^2) for 10 min 24 h after intravenous injection with MSNs@Ce6. For the simultaneous administration, the CAFs-rich H22 tumor-bearing mice were intravenously administrated with MSNs@Ce6 on day 0 and day 3, and intravenously injected with AEAA-MSNs@RA/GA on day 0, day 3, day 6 and day 9. For the sequential administration, the CAF-rich H22 tumor-bearing mice were intravenously injected with AEAA-MSNs@RA/GA on day 0, day 3, day 6 and day 9, and intravenously injected with MSNs@Ce6 on day 11 and day 13. The mice were weighed every 3 days. The tumor size in each group was measured using a digital caliper every 3 days, and the tumor volume was calculated using the following equation: tumor volume = 0.52 × tumor length × tumor width^2. All the mice were sacrificed on day 21. Then, these tumors were harvested, weighed, formalin-fixed and sliced for immunofluorescent staining. The serum was collected and analyzed using the Elisa kits. The major organs were harvested and fixed for hematoxylin and eosin (HE) staining.

Statistical Analysis

Student's test was utilized to analyze the statistical differences of the data. The differences among the different groups were compared by analysis of variance (ANOVA).

Results and Discussion

MSNs were synthesized by using a previously reported sol–gel method.[24,25] Transmission electron microscopy (TEM) revealed a uniformly spherical structure of the prepared MSNs with a diameter of approximate 80 nm (Figure 1A). The N$_2$ adsorption/desorption isotherms in Figure 1B and C indicated that the MSNs had a large pore volume (0.61 cm^3/g), high BET
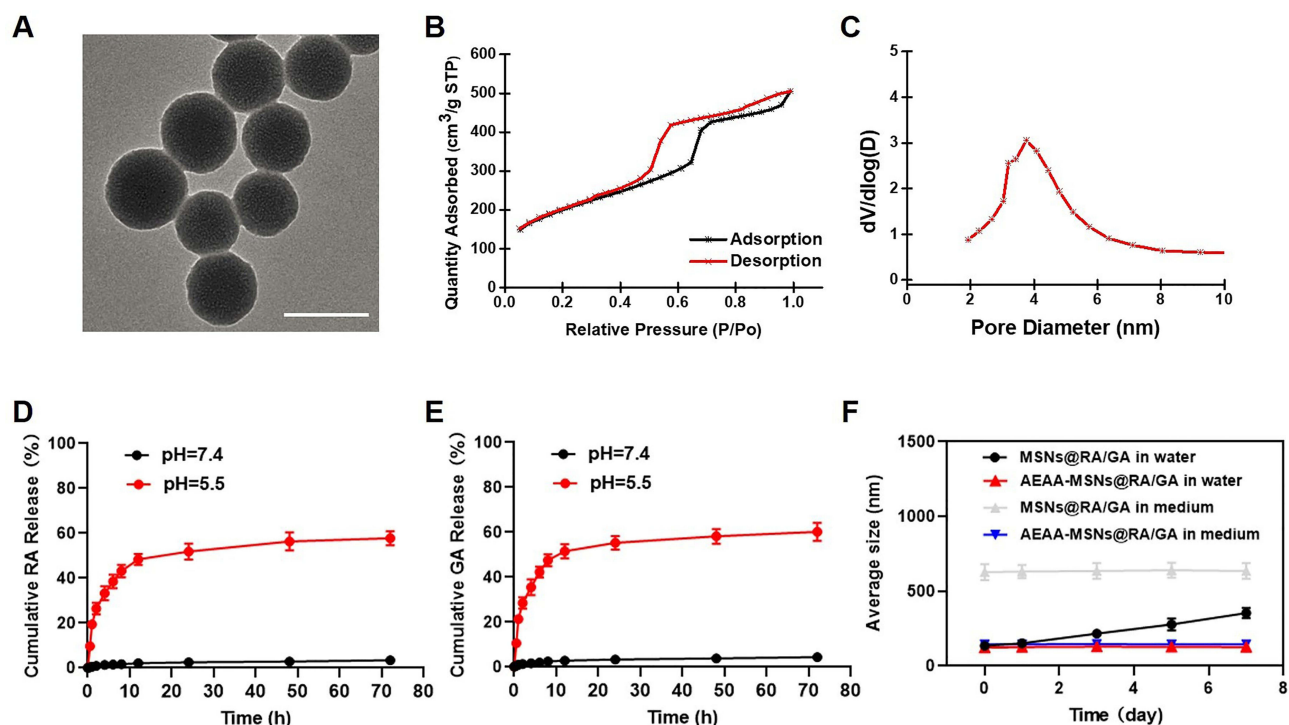

Figure 1 Preparation, characterization and drug release of AEAA-MSNs@RA/GA. (**A**) TEM image of MSNs, the scale bar = 100 nm. (**B**) N$_2$ adsorption−desorption isotherms of MSNs. (**C**) Pore size distribution of MSNs. (**D**) Cumulative RA release from AEAA-MSNs@RA/GA. (**E**) Cumulative GA release from AEAA-MSNs@RA/GA. (**F**) Average size of AEAA-MSNs@RA/GA and AEAA-MSNs@RA/GA after stockage in deionized water and RPMI-1640 medium for 0, 1, 3, 5 and 7 days, n = 3. Data are presented as mean ± SD.

surface area (854.3 m2/g) and well-defined pore size (2.7 nm), which facilitated drug loading. Thereafter, we functionalized the amino groups onto the MSNs to improve the drug loading ability, and subsequently investigated the drug loading content and release properties of MSNs. Both RA and GA were co-loaded into MSNs, and the drug loading content of RA and GA were $10.2 \pm 0.3\%$ and $8.1 \pm 0.2\%$, respectively. The RA/GA-co-loaded MSNs (MSNs@RA/GA) exhibited a spherical structure and slightly smaller pore size distribution than unloaded MSNs (Figure S1). Furthermore, RA/GA-co-loaded MSNs (MSNs@RA/GA) showed a pH-responsive drug release manner, in which >55% of RA and >60% of GA were released at pH 5.5 in comparison to <4% of RA and <5% of GA release at pH 7.4 (Figure 1D and E). This pH-responsive release behavior was beneficial for cancer therapy because the extracellular TME and intracellular lysosomes are acidic. Since aminoethyl anisamide (AEAA) is considered a targeting ligand of sigma receptor that is overexpressed on the surface of CAFs, AEAA-polyethylene glycol (PEG) amine was conjugated onto the surface of carboxyl-functionalized MSN to improve the CAF targeting of the nanoparticles. These AEAA-modified MSNs@RA/GA (AEAA-MSNs@RA/GA) exhibited no significant change in size during one-week storage period in cell medium and pure water, whereas aggregation occurred in the bare MSNs@RA/GA (Figure 1F), suggesting that PEGylation improved the stability of MSNs@RA/GA.

To investigate the CAF-targeted effect of AEAA-MSNs, we first generated CAFs through stimulating NIH/3T3 cell differentiation by using TGF/β1. The CAFs were confirmed by the high mRNA expression of α-SMA and FAP- α, which are the specific biomarkers of CAFs (Figure 2A and B). Subsequently, we detected the cellular internalization of Cy 5.5-labeled MSNs and AEAA-MSNs in CAFs and H22 cells by using CLSM and flow cytometry. As shown in Figure 2C-F, both cell lines are effectively phagocytosed AEAA-MSNs and MSNs after 6 h of incubation. Furthermore, more notable fluorescent signals were observed in CAFs after treatment with AEAA-MSNs than those treated with non-targeted MSNs, whereas both AEAA-MSNs and MSNs exhibited a similar cellular uptake efficiency in the H22 cells. The results of flow cytometry were consistent. These results confirmed that AEAA-modified MSNS enhanced the CAF targeting. Then, cytotoxicity of AEAA-MSNs and AEAA-MSNs@RA/GA from 0 to 100 mg/mL was evaluated in CAFs, H22 cells and HUVECs using SRB assays. Negligible cytotoxicity of AEAA-MSNs was observed in the three cell lines (Figure 2G-I), indicating good biosafety of the AEAA-MSNs. Additionally, AEAA-MSNs@RA/GA showed concentration-dependent toxicity towards CAFs, H22 cells and HUVECs, and the killing effect of AEAA-MSNs@RA/GA in CAFs was stronger than those in H22 cells and HUVECs, which was possibly due to the preferable endocytosis in CAFs. Studies have indicated that the elimination of CAFs increases the risk of cancerous invasion or migration.[26,27] To avoid this risk, AEAA-MSNs @RA/GA are expected to regulate CAFs without decreasing the cell viability. Therefore, we opted 12.5 μg/mL of AEAA-MSNs@RA/GA as an optimal concentration for the subsequent experiments because the cell viability of CAFs was above than 90% when the concentration was ≥12.5 μg/mL. Encouragingly, free RA, AEAA-MSNs@RA/GA and AEAA-MSNs @RA effectively transformed activated CAFs into a quiescent state, as indicated by the decreased expression of α-SMA and FAP-α in the CAFs (Figure 3A and B). However, no obvious change in the expression of α-SMA and FAP-α was observed in the cells treated with free GA, AEAA-MSNs or AEAA-MSNs@GA, suggesting that AEAA-MSNs and GA had no effect on the inactivation of CAFs. The reversal of activated CAFs by AEAA-MSNs@RA/GA was further investigated in vivo using an H22 mouse hepatocellular carcinoma model. After tail vein injection, AEAA-MSNs@RA/GA was predominantly distributed in the liver, spleen kidneys of the reticuloendothelial system and tumor tissues, and their accumulation efficiency in tumor tissues peaked after 6 h of administration (Figure 3D and E), indicating the rapid accumulation of AEAA-MSNs @RA/GA within the TME. More importantly, AEAA-MSNs@RA/GA markedly decreased the α-SMA and FAP-α positive CAFs, confirming the ability of AEAA-MSNs@RA/GA to reprogram the activated CAFs into quiescence. Due to the inactivation of CAFs, AEAA-MSNs@RA/GA decreased the production of collagen in the TME (Figure 3D and E), which contribute to overcome the protective barrier formed by the dense collagen and alleviate the pressure on the tumor vessels.

To investigate the effect of AEAA-MSNs@RA/GA on tumor vessels, two proangiogenic genes (VEGFA and EGF) and two vascular maturation-related genes (ANGPT1 and S1PR1) were evaluated in HUVECs after treatment with various formulations. As shown in Figure 4A-D, free GA, AEAA-MSNs@GA and AEAA-MSNs@RA/GA significantly down-regulated the mRNA expression of VEGFA and EGF while upregulating the mRNA expression of ANGPT1 and S1PR1. However, free retinoic acid, AEAA-MSNs and AEAA-MSNs@RA had no effect on the expression of the four genes. These results indicated that AEAA-MSNs@RA/GA could transform pro-angiogenic HUVECs to the vascular-stabilizing pheno-type. To further explore whether AEAA-MSNs@RA/GA could induce tumor vasculature normalization, the tumor sections
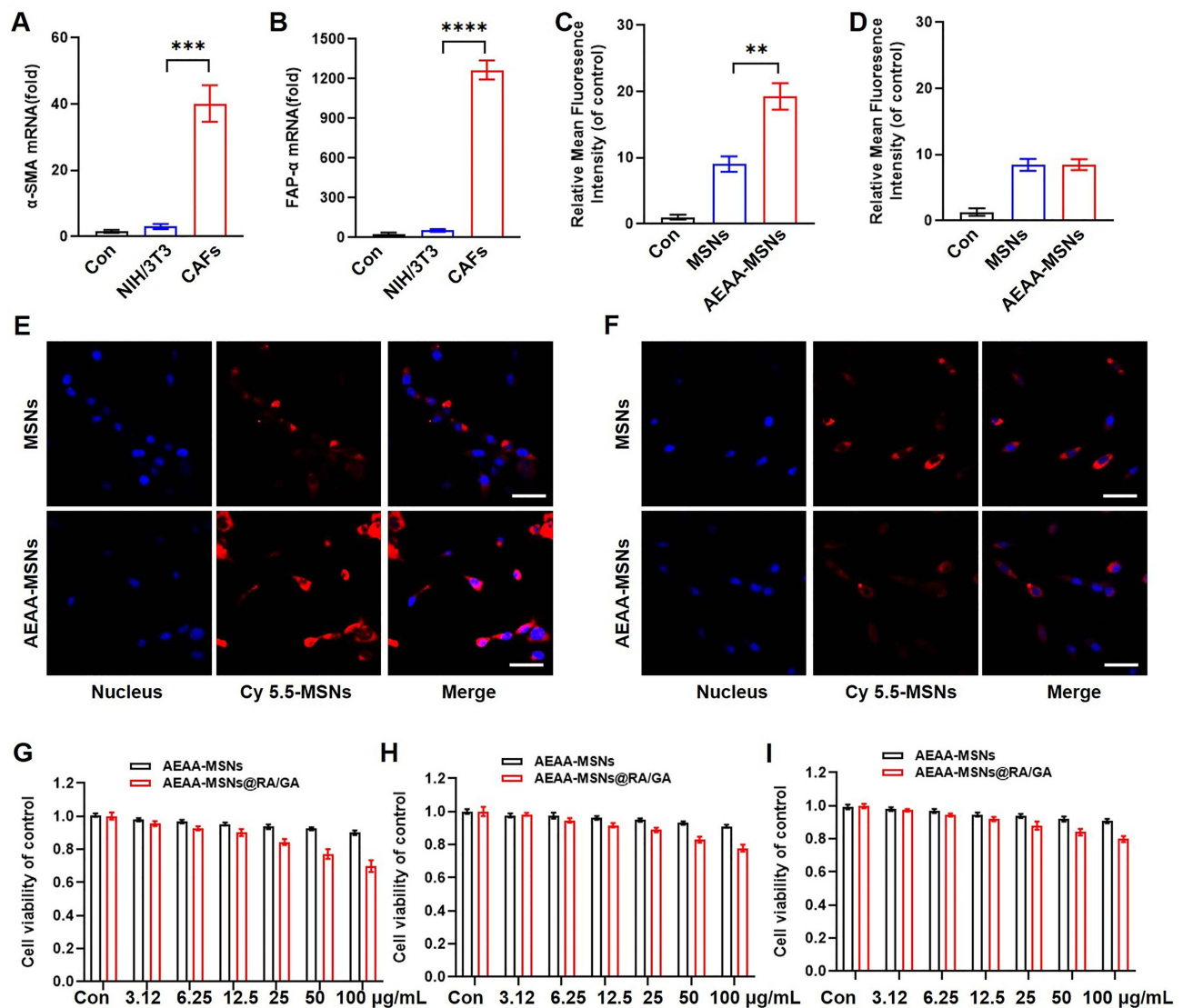
Figure 2 Endocytosis and cytotoxicity. (**A and B**) The expression level of (**A**) α-SMA mRNA and (**B**) FAP-α mRNA detected by qPCR, GAPDH was used as the control group. (**C and D**) Quantitative FACS analysis of cellular uptake of AEAA-MSNs and MSNs in (**C**) CAFs and (**D**) H22 cells, n = 3. (**E and F**) CLSM images of (**E**) CAFs and (**F**) H22 cells after co-incubation with AEAA-MSNs or MSNs for 6 h, the scale bar = 10 μm. (**G-I**) Cytotoxicity of AEAA-MSNs and AEAA-MSNs@RA/GA against (**G**) CAFs, (**H**) H22 cells and (**I**) HUVECs at various concentrations, n = 4. All the data are presented as mean ± SD. **$P < 0.01$, ***$P < 0.005$, ****$P < 0.001$.

of mice after various treatments were stained with anti-CD31, anti-VE-cadherin and anti-ICAM-1 antibodies to evaluate the structural and functional features of tumor vasculatures. As shown in Figure 4E and F, AEAA-MSNs had negligible effects on the vasculature structure and functions compared with the saline treatment groups. In contrast, AEAA-MSNs@RA/GA induced the structural normalization of tumor vasculatures, including length reduction and a decrease in heterogeneity. Moreover, the higher expression of VE-cadherin and ICAM-1 was observed in the tumor sections of mice treated with AEAA-MSNs@RA/GA than that treated with saline, indicating that an increase in the integrity of the VE-cadherin-constituted adhesive junction and the trans-endothelial migration of lymphocytes, which suggested that AEAA-MSNs @RA/GA improved the functionality of tumor vasculatures. Notably, AEAA-MSNs@RA/GA showed a higher vascular normalization efficiency than AEAA-MSNs@GA, the reason of which was attributed to the inhibition of ECM secretion by the loaded RA and thus subsequently decreasing the tumoral solid stress to compress vessels.

Hypoxia within the TME is one of the most crucial factors driving tumorigenesis and restricting the therapeutic efficiency of PDT. AEAA-MSNs@GA were expected to recover tumor oxygen transport by breaking the physical barrier of the TME and promoting vascular normalization. Therefore, the hypoxic status of tumors after various treatments was investigated using
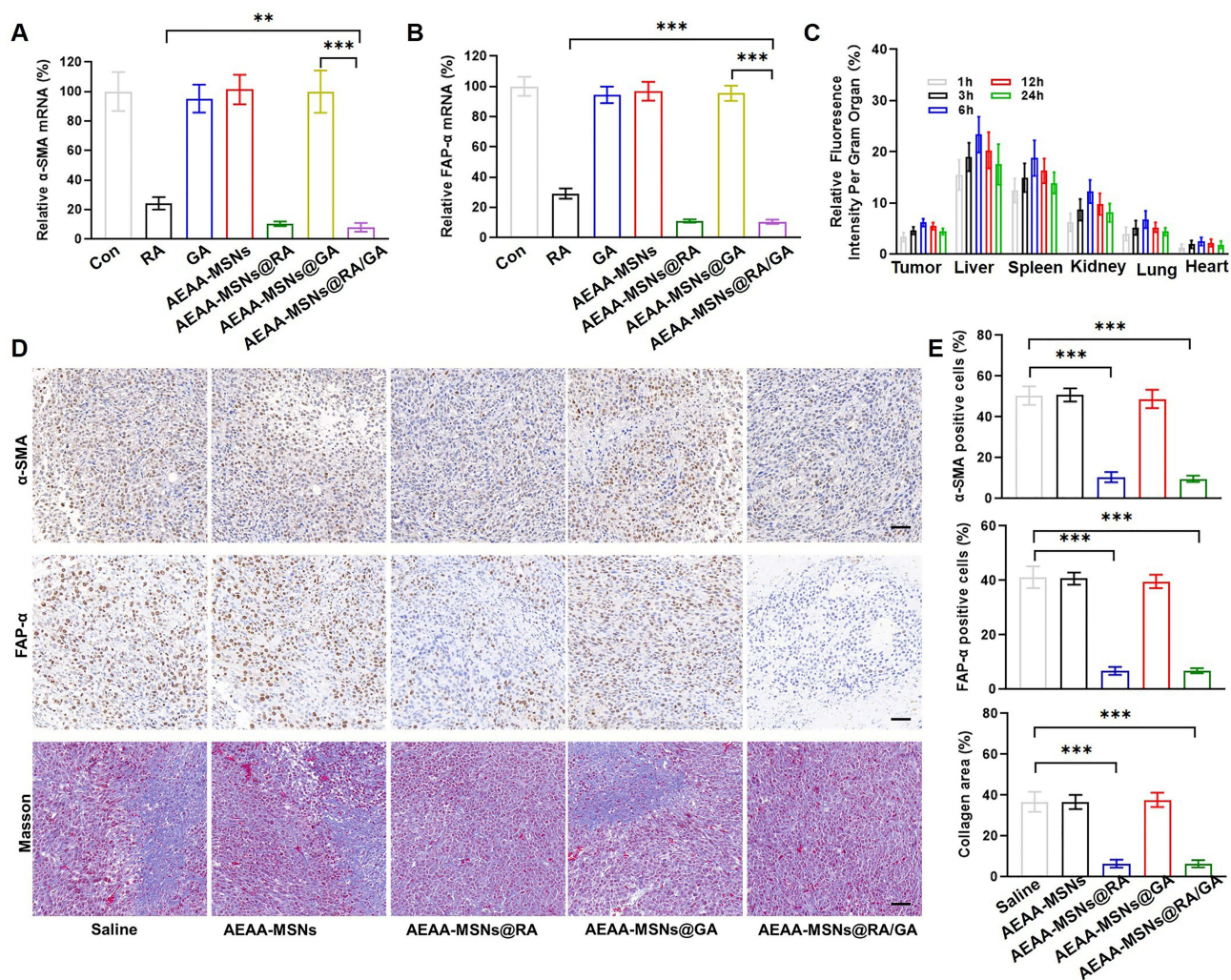
Figure 3 The reversal of activated CAFs. (**A** and **B**) Relative expression of (**A**) α-SMA mRNA and (**B**) FAP-α mRNA in CAFs after incubated with various formulation detected by qPCR, n = 3, *P < 0.05, **P < 0.01, ***P < 0.005. (**C**) Biodistribution of AEAA-MSNs@RA/GA at various time point post intravenous injection, n=4. (**D**) Immunohistochemical staining of α-SMA (upper), FAP-α (middle) and collagen (down) in CAFs after various treatments, the scale bar = 100 μ m. (**E**) Quantitative analysis of α-SMA (upper), FAP-α (middle) and collagen (down) in CAFs after various treatments, n = 3. All the data are presented as mean ± SD. **P < 0.01, ***P < 0.005.

a hypoxic dye. Compared with the saline and AEAA-MSNs groups, AEAA-MSNs@RA and AEAA-MSNs@GA led to an obvious decrease of the hypoxia-associated fluorescence signals in the tumor section. As expected, AEAA-MSNs@RA/GA showed the strongest ability to attenuate tumor hypoxia through the combined effects of CAF regulation and vascular normalization. These results suggested that AEAA-MSNs@RA/GA could improve the therapeutic efficacy of PDT through relieving tumor hypoxia. Another obstacle of PDT is the limited entry of photosensitizers into the tumors due to the excessive stroma and defective vessels. Therefore, we investigated whether AEAA-MSNs@RA/GA could improve the tumor accumulation efficiency of photosensitizers through reprogramming the TME. Chlorine e6 (Ce6) is a widely used photosensitizer. Considering its poor aqueous solubility and rapid blood clearance, Ce6 was loaded into the PEGylated MSNs (MSNs@Ce6) to improving its bioavailability. As shown in Figure S2, the prepared MSNs@Ce6 showed a uniform morphology, high Ce6 loading content (13.2%) and Ph-responsive release manner as well as long-term stability in water and cell medium. Furthermore, MSNs@Ce6 induced a negligible cell death of H22 cells, whereas exhibiting a concentration-dependent cytotoxicity towards H22 cells at the presence of the 660 nm laser irradiation (Figure S3), confirming that MSNs@Ce6 could be used as effective photosensitizers. Then, the accumulation of Cy5.5-labeled MSNs@Ce6 was detected in the tumors of CAF-rich H22 tumor-bearing mice after various treatments. As shown in Figure S4, MSNs@Ce6 accumulated at tumor sites through the enhanced permeability and retention (EPR) effect and the tumoral accumulation peaked around 24 h after
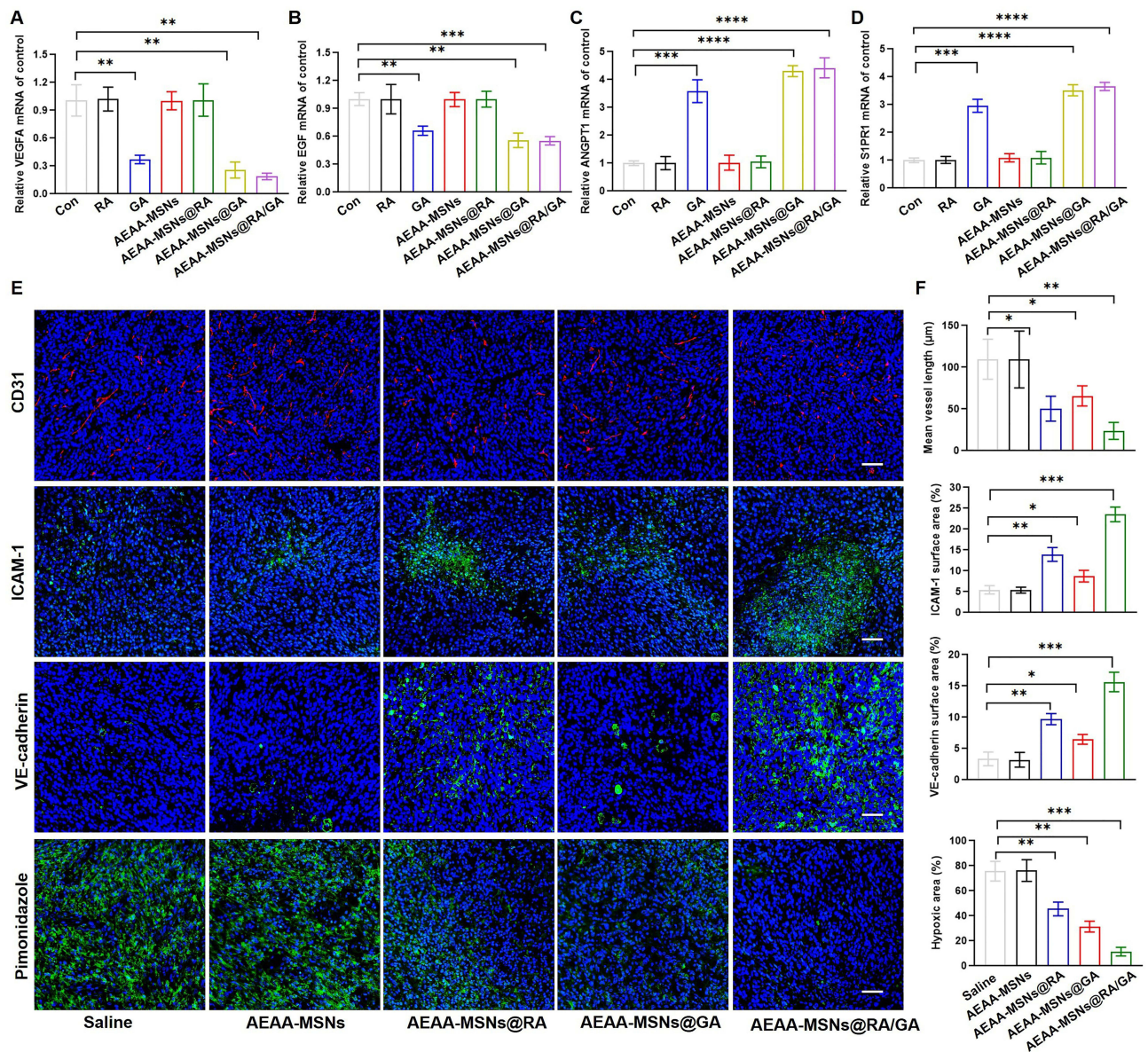
Figure 4 Tumor vasculature normalization. (**A-D**) Relative expression of the proangiogenic (**A**) VEGFA and (**B**) EGF mRNA and vascular maturation-related (**C**) ANGPT1 mRNA and (**D**) S1PR1 mRNA in HUVECs after various treatments, n = 3. (**E**) Tumor slices were stained with anti-CD31, anti-ICAM-1, anti-VE-cadherin and anti-pimonidazole after various treatments, respectively, the scale bar = 100 μm. (**F**) Mean vessel length and the positive area of ICAM-1, VE-cadherin and hypoxia in tumor slices after various treatments analyzed by ImageJ, n =3. All the data are presented as mean ± SD. *P < 0.05, **P < 0.01, ***P < 0.005, ****P < 0.001.

intravenous injection. More importantly, the accumulation efficiency of MSNs@Ce6 in the AEAA-MSNs@RA/GA-pretreated mice was promoted by 1.9-fold compared with that in the saline-pretreated mice, which was significantly higher than those in the AEAA-MSNs -pretreated mice (1.0-fold), AEAA-MSNs@RA -pretreated mice (1.4-fold) and AEAA-MSNs @GA-pretreated mice (1.3-fold). These results indicated that the combination of CAF regulation and vascular normalization improved the accumulation efficiency of nanodrugs within solid tumors, which might overcome the therapeutic resistance of PDT by the physic barriers.

We further investigated the ability of AEAA-MSNs@RA/GA to enhance the therapeutic efficacy of PDT in vivo. Thereafter, we examined the antitumor effects from two types of combination treatments, simultaneous administration of AEAA-MSNs@RA/GA with MSNs@Ce6 and sequential administration of AEAA-MSNs@RA/GA with MSNs@Ce6, in CAF-rich H22 mouse tumor models. As shown in Figure 5A-C, MSNs@Ce6 plus the laser showed an unsatisfactory inhibitory effect on tumor growth due to the therapeutic resistance from the TME. Additionally, AEAA-MSNs@RA/GA
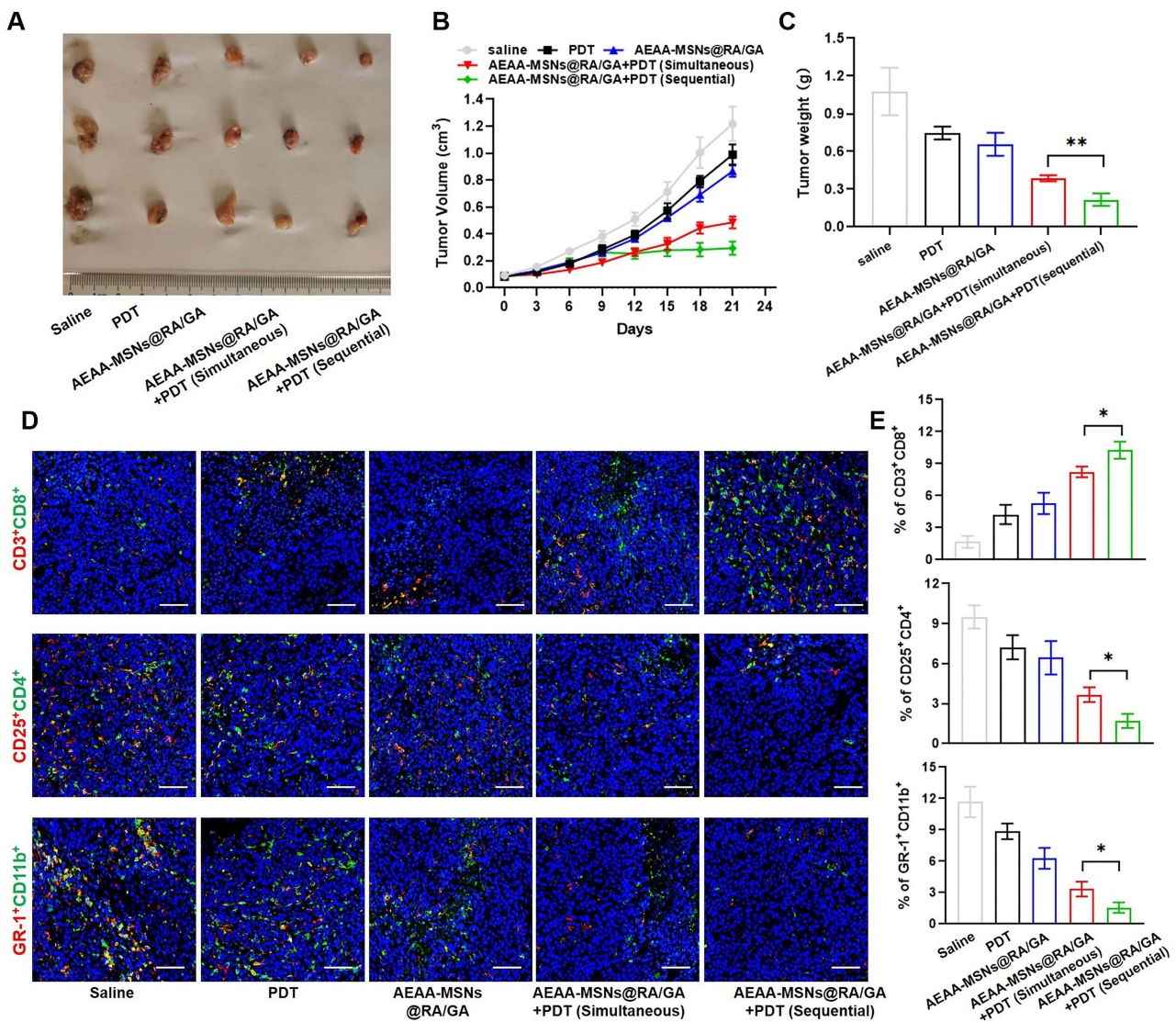
Figure 5 In vivo therapeutic effect and immune microenvironment regulation. (**A**) tumor images. (**B**) tumor volumes. (**C**) tumor weights. (**D**) immunofluorescence analysis of CD 8^{+} T cells (CD8: red, CD3: green), Tregs (CD25: red, CD4: green) and MDSCs (GR-1: red, CD11b: green) infiltrated in tumor, the scale bar = 100 μm. (**E**) CD 8^{+} T cells, Tregs, and MDSCs to total cells in the same tumor areas, n = 3. Data are presented as mean ± SD. *P < 0.05, **P < 0.01.

delayed tumor volume growth and weight increase, which was because the reversal of activated CAFs and vascular normalization decreased the malignant degree of tumor. Compared with the single AEAA-MSNs@RA/GA or single PDT, the two types of the combination of AEAA-MSNs@RA/GA with PDT led to lower tumor volume and weight. Furthermore, sequential administration profiles exhibited a better synergistic effect than simultaneous profiles. It can be explained that the first administration of AEAA-MSNs@RA/GA alleviated tumor hypoxia and improved tumor penetrability after three successive treatments, creating a favorable TME for the subsequent PDT. These results confirmed that the sequential treatment strategy of the CAF regulation and tumor vasculature normalization prior to the PDT could effectively potentiate the subsequent PDT of cancer.

Extensive studies have highlighted that the use of PDT as anticancer vaccine can recruit and alert immune cells through the exposure and secretion of danger molecules.[28–30] However, activated CAFs can interact with tumor-infiltrating immune cells by secreting various cytokines, chemokines, and other effector molecules, which remodels an immunosuppressive TME and thus bestows cancer cells to evade the surveillance of the immune system.[31,32] Furthermore, abnormal tumor blood vessel limited tumor infiltration of immune cells and also facilitated immune

evasion.[13,33] By immunohistochemistry (IHC) analysis, we found that PDT alone induced an unsatisfactory enhancement in the tumor infiltration of CD8+ T cells and reduction in the tumor infiltration of immunosuppressive regulatory T cells (Tregs) and myeloid-derived suppressor cells (MDSCs) compared with the saline groups (Figure 5D and E). Additionally, AEAA-MSNs@RA/GA alleviated the immunosuppressive TME due to the inactivation of CAFs and tumor vessel normalization. As expected, the combination of AEAA-MSNs@RA/GA with PDT increased the tumoral infiltration of CD8+ T cells, but decreased the ratio of Tregs and MDSCs in comparison to the single PDT or the single AEAA-MSNs@RA/GA. Consistent with the results of the antitumor effect, sequential administration profiles resulted in more CD8+ T cells, and fewer Tregs and MDSCs than simultaneous profiles within the TME. Furthermore, sequential administration triggered the most pronounced inflammatory cytokine production including TNF-α and IFN-γ (Figure S5). These results indicated that AEAA-MSNs@RA/GA could effectively improve the antitumor immune response of PDT through favoring immunostimulatory cells over immunosuppressive cells.

We subsequently measured the body weight of these mice after various treatments every three 3 days. There was negligible weight loss in all the treatment groups in comparison to the control groups (Figure 6A). The serum biochemistry indexes, including alkaline phosphatase (ALP), alanine transaminase (ALT), aspartate transaminase (AST), blood urea nitrogen (BUN), and creatinine (CRE), were examined to evaluate the liver and kidney functions (Figure 6B-F). No apparent changes of the serum biochemistry indexes were observed during the treatments. Furthermore, H&E staining indicated no observable pathological injuries of major organs in all the treatment groups (Figure 6G). These results demonstrated the low systemic toxicity of the combination therapies.
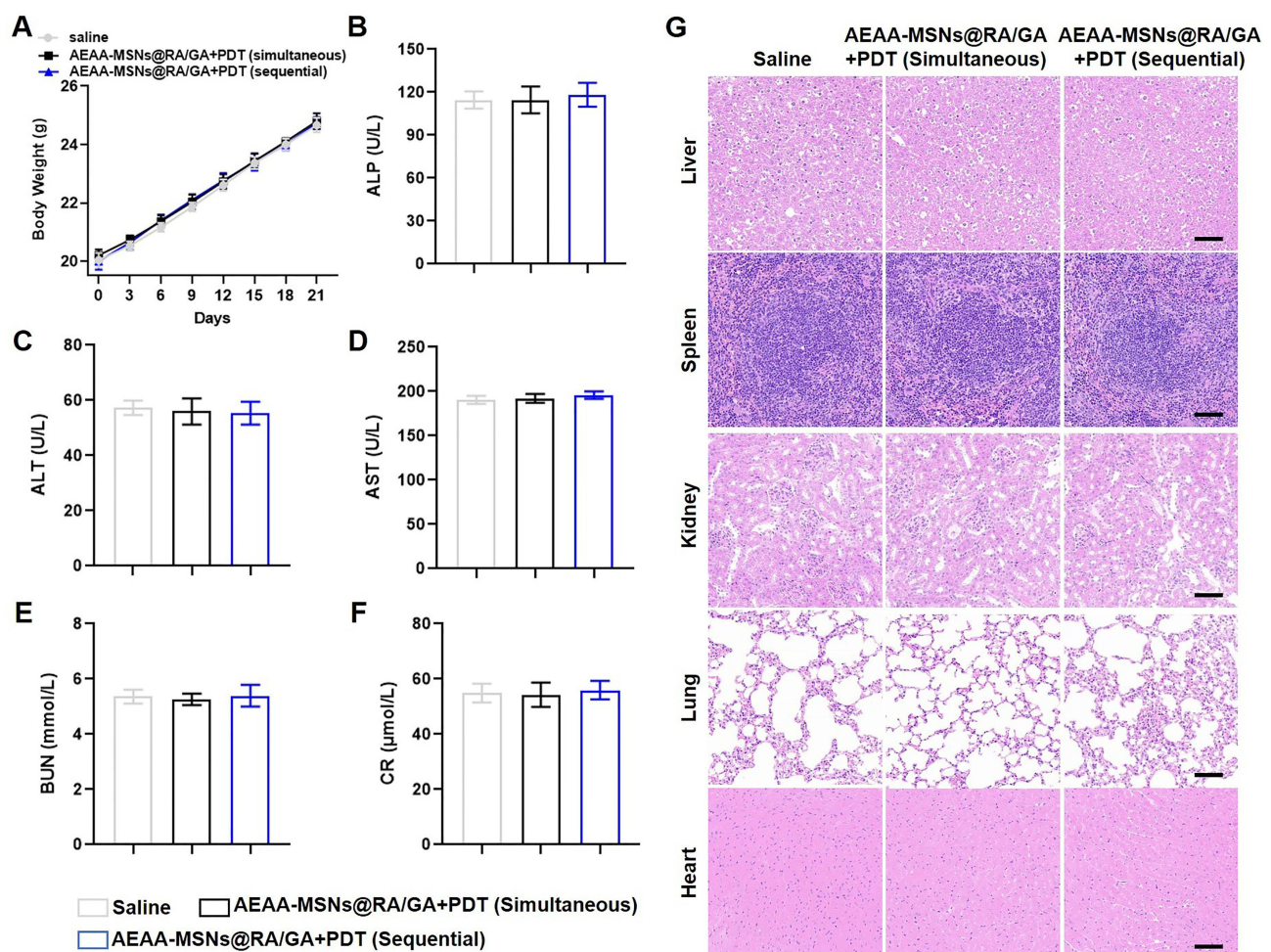
Figure 6 Biosafety of combined therapies. (**A**) Body weights, n =3 (**B-F**) Analysis of serum biochemical indicators including (**B**) ALP, (**C**) ALT, (**D**) AST, (**E**) BUN, (**F**) CR in each group, n = 3. All the data are presented as mean ± SD. (**G**) H&E staining of the major organs, the scale bar = 50 μm.

Conclusion

In summary, AEAA-modified MSNs were fabricated to deliver RA and gambogic acid GA. The prepared AEAA-MSNs @RA/GA showed high drug loading content and pH-responsive release properties. Due to the modification of PEG-conjugated AEAA, AEAA-MSNs@RA/GA exhibited a good stability and high cellular internalization with CAFs, which prolonged the blood clearance of RA and GA and improved their tumor accumulation. After optimizing the concentration, AEAA-MSNs@RA/GA transformed the activated CAFs into quiescent cells and restored the tumor vasculatures without decreasing the viability of CAFs and vascular endothelial cells, thus reducing collagen deposition, alleviating TME hypoxia and improving the subsequent tumor accumulation efficiency of the photosensitizers. In vivo experiments demonstrated that AEAA-MSNs@RA/GA effectively potentiated the efficacy of PDT, and sequential administration of AEAA-MSNs@RA/GA followed by photosensitizers showed a better antitumor effect than simultaneous administration of AEAA-MSNs@RA/GA and photosensitizers. More importantly, AEAA-MSNs@RA/GA regulated the immunosuppressive TME through improving the infiltration of immunostimulatory cells such as CD 8+T cell while decreasing the immunosuppressive Tregs and MDSCs, which further strengthened the PDT-induced immune response. Collectively, AEAA-MSNs@RA/GA could create a favorable TME for PDT by reversing the activated CAFs and normalizing tumor vasculatures, which might be a promising candidate for sensitizing the PDT of liver cancer in a sequential manner.

Acknowledgments

Disclosure

The authors report no conflicts of interest in this work.

References

1. Llovet JM, Castet F, Heikenwalder M., et al. Immunotherapies for hepatocellular carcinoma. *Nat Rev Clin Oncol*. 2022;19(3):151–172.
2. Bosch FX, Ribes J, Cléries R, Díaz M. Epidemiology of hepatocellular carcinoma. *Clin Liver Dis*. 2005;9(2):191–211.
3. Kelley RK, Greten TF. Hepatocellular carcinoma—origins and outcomes. *N Eng J Med*. 2021;385(3):280–282.
4. Anwanwan D, Singh SK, Singh S, Saikam V, Singh R. Challenges in liver cancer and possible treatment approaches. *Biochimica et Biophysica Acta*. 2020;1873(1):188314.
5. Wulf J, Guckenberger M, Haedinger U, et al. Stereotactic radiotherapy of primary liver cancer and hepatic metastases. *Acta oncologica*. 2006;45 (7):838–847.
6. Pham TC, Nguyen V-N, Choi Y, Lee S, Yoon J. Recent strategies to develop innovative photosensitizers for enhanced photodynamic therapy. *Chem Rev*. 2021;121(21):13454–13619.
7. Dos Santos A, de Almeida DQ, Terra LF, Baptista M, Labriola L. Photodynamic therapy in cancer treatment-an update review. *J Cancer Metastasis Treat*. 2019;5(25):10.20517.
8. Hou G, Qian J, Guo M, et al. Copper coordinated nanozyme-assisted photodynamic therapy for potentiating PD-1 blockade through amplifying oxidative stress. *Chem Eng J*. 2022;435:134778.
9. Ji B, Wei M, Yang B. Recent advances in nanomedicines for photodynamic therapy (PDT)-driven cancer immunotherapy. *Theranostics*. 2022;12 (1):434.
10. Wan Y, Fu LH, Li C, Lin J, Huang P. Conquering the hypoxia limitation for photodynamic therapy. *Adv Mater*. 2021;33(48):2103978.
11. Zhang C, Qin W-J, Bai X-F, Zhang X-Z. Nanomaterials to relieve tumor hypoxia for enhanced photodynamic therapy. *Nano Today*. 2020;35:100960.
12. Wang Y, Xu Y, Guo X, et al. Enhanced antimicrobial activity through the combination of antimicrobial photodynamic therapy and low-frequency ultrasonic irradiation. *Adv Drug Deliv Rev*. 2022;114168.
13. Liu Z, Wang Y, Huang Y, et al. Tumor vasculatures: a new target for cancer immunotherapy. *Trends Pharmacol Sci*. 2019;40(9):613–623.
14. Chen Y, Liu X, Yuan H, et al. Therapeutic remodeling of the tumor microenvironment enhances nanoparticle delivery. *Adv Sci*. 2019;6(5):1802070.
15. Matuszewska K, Pereira M, Petrik D, Lawler J, Petrik J. Normalizing tumor vasculature to reduce hypoxia, enhance perfusion, and optimize therapy uptake. *Cancers*. 2021;13(17):4444.
16. Gao F, Yang C. Anti-VEGF/VEGFR2 monoclonal antibodies and their combinations with PD-1/PD-L1 inhibitors in clinic. *Curr Cancer Drug Targets*. 2020;20(1):3–18.
17. Huang Y, Goel S, Duda DG, Fukumura D, Jain RK. Vascular Normalization as an Emerging Strategy to Enhance Cancer ImmunotherapyVascular Normalization to Boost Immunotherapy. *Cancer Res*. 2013;73(10):2943–2948.
18. Huang Y, Chen Y, Zhou S, et al. Dual-mechanism based CTLs infiltration enhancement initiated by Nano-sapper potentiates immunotherapy against immune-excluded tumors. *Nat Commun*. 2020;11(1):622.
19. Deng Y, Jiang Z, Jin Y, et al. Reinforcing vascular normalization therapy with a bi-directional nano-system to achieve therapeutic-friendly tumor microenvironment. *J Controlled Release*. 2021;340:87–101.

20. Chen Y, McAndrews KM, Kalluri R. Clinical and therapeutic relevance of cancer-associated fibroblasts. *Nat Rev Clin Oncol.* 2021;18(12):792–804.
21. Shen W, Yao P-A, Li W, et al. Cancer-associated fibroblast-targeted nanodrugs reshape colorectal tumor microenvironments to suppress tumor proliferation, metastasis and improve drug penetration. *J Materials Chem B*. 2023.
22. Wu F, Yang J, Liu J, et al. Signaling pathways in cancer-associated fibroblasts and targeted therapy for cancer. *Signal Transduction Targeted Therapy.* 2021;6(1):218.
23. Shiga K, Hara M, Nagasaki T, Sato T, Takahashi H, Takeyama H. Cancer-associated fibroblasts: their characteristics and their roles in tumor growth. *Cancers.* 2015;7(4):2443–2458.
24. Yang C, He Y, Chen F, Zhang F, Shao D, Wang Z. Leveraging n-Adrenergic Receptor Signaling Blockade for Improved Cancer Immunotherapy Through Biomimetic Nanovaccine. *Small.* 2023;19(14):2207029.
25. Trewyn BG, Slowing II, Giri S. Synthesis and functionalization of a mesoporous silica nanoparticle based on the sol–gel process and applications in controlled release. *Acc Chem Res.* 2007;40(9):846–853.
26. Yamaguchi H, Sakai R. Direct interaction between carcinoma cells and cancer associated fibroblasts for the regulation of cancer invasion. *Cancers.* 2015;7(4):2054–2062.
27. Lang J, Zhao X, Qi Y, et al. Reshaping prostate tumor microenvironment to suppress metastasis via cancer-associated fibroblast inactivation with peptide-assembly-based nanosystem. *ACS nano.* 2019;13(11):12357–12371.
28. Garg AD, Nowis D, Golab J, Agostinis P. Photodynamic therapy: illuminating the road from cell death towards anti-tumour immunity. *Apoptosis.* 2010;15:1050–1071.
29. Doix B, Trempolec N, Riant O, Feron O. Low photosensitizer dose and early radiotherapy enhance antitumor immune response of photodynamic therapy-based dendritic cell vaccination. *Front Oncol.* 2019;9:811.
30. Alzeibak R, Mishchenko TA, Shilyagina NY, Balalaeva IV, Krysko DV. Targeting immunogenic cancer cell death by photodynamic therapy: past, present and future. *J Immunother Cancer.* 2021;9(1):46.
31. Mao X, Xu J, Wang W, et al. Crosstalk between cancer-associated fibroblasts and immune cells in the tumor microenvironment: new findings and future perspectives. *Mol Cancer.* 2021;20(1):1–30.
32. Zhu Y, Li X, Wang L, Hong X, Yang J. Metabolic reprogramming and crosstalk of cancer-related fibroblasts and immune cells in the tumor microenvironment. *Front Endocrinol.* 2022;13:988295.
33. Missiaen R, Mazzone M, Bergers G The reciprocal function and regulation of tumor vessels and immune cells offers new therapeutic opportunities in cancer. Paper presented at: Seminars in cancer biology; 2018.